J. Geogr. Sci. 2023, 33(12): 2530-2548
DOI: https://doi.org/10.1007/s11442-023-2188-5

Evaluating flash flood simulation capability with respect to rainfall temporal variability in a small mountainous catchment

WANG Xuemei[1], *ZHAI Xiaoyan[1], ZHANG Yongyong[2], GUO Liang[1]

1. State Key Laboratory of Simulation and Regulation of Water Cycle in River Basin, Research Center on Flood and Drought Disaster Reduction, China Institute of Water Resources and Hydropower Research, Beijing 100038, China;
2. Key Laboratory of Water Cycle and Related Land Surface Processes, Institute of Geographic Sciences and Natural Resources Research, CAS, Beijing 100101, China

Abstract: Rainfall temporal patterns significantly affect variability of flash flood behaviors, and further act on hydrological model performances in operational flash flood forecasting and warning. In this study, multivariate statistical analysis and hydrological simulations (XAJ and CNFF models) were combined to identify typical rainfall temporal patterns and evaluate model simulation capability for water balances, hydrographs, and flash flood behaviors under various rainfall patterns. Results showed that all the rainfall events were clustered into three types (Type 1, Type 2, and Type 3) in Anhe catchment in southeastern China. Type 1 was characterized by small total amount, high intensity, short duration, early peak moment, and concentrated hourly distribution. Type 3 was characterized by great total amount, low intensity, long duration, late peak moment, and uniform hourly distribution. Characteristics of Type 2 laid between those of Type 1 and Type 3. XAJ and CNFF better simulated water balances and hydrographs for Type 3, as well as all flash flood behavior indices and flood dynamics indices. Flood peak indices were competitively simulated for all the types by XAJ and except Type 1 by CNFF. The study is of significance for understanding relationships between rainfall and flash flood behaviors and accurately evaluating flash flood simulations.

Keywords: rainfall characteristic indices; flash flood behavior indices; hydrological model; mountainous catchment

1 Introduction

Flash floods are defined as the intense catchment responses to rainfall storms in mountainous catchments, which are characterized by extremely sudden onset, rapid flood response, and highly concentrated flood energy (Ritter *et al*., 2020; Leal *et al*., 2022; Habibi *et al*., 2023). They are recognized as the main flood disasters causing grave losses of life and

Received: 2022-12-27 **Accepted:** 2023-09-26
Foundation: National Natural Science Foundation of China, No.42171047, No.42071041
Author: Wang Xuemei (1998–), PhD Candidate, specialized in hydrology and water resources. E-mail: wang_xmww@163.com
***Corresponding author:** Zhai Xiaoyan (1989–), Associate Professor, specialized in hydrology and water resources. E-mail: zhaixy@iwhr.com

property (Khajehei *et al*., 2020). Globally, property losses caused by flash flood disasters is the most prominent among natural disasters (Borga *et al*., 2011; Yin *et al*., 2023), and 40%–90% of flood-related casualties are owing to flash floods (Barredo, 2007; Ashley and Ashley, 2008; Zhai *et al*., 2021a). China is one of the countries seriously affected by flash flood disasters worldwide. Flash floods accounts for more than 70% of the flood-related casualties, and the annual direct economic losses have exceeded 120 billion CNY from 2000 to 2017 (Zhang *et al*., 2019; Zhai *et al*., 2021a). Identifying rainfall-flood response regularities and developing effective flash flood forecasting techniques can provide scientific supports for decision making of flash flood disaster prevention, as well as timely release of flash flood warning information.

Short-duration heavy rainfall is widely accepted as the direct inducing force of flash floods (Garambois *et al*., 2014; Lompi *et al*., 2022). Catchment hydrological responses involving runoff generation and concentration processes are sensitive to the temporal structure of rainfall forcing, which can be reflected by the variations of flood characteristics (e.g., timing, magnitude, and shape) (Batisani, 2011; Zhang *et al*., 2020; Liu *et al*., 2022). Series of studies have been conducted to investigate the relationships between flood characteristics and rainfall temporal distributions. Brunner *et al*. (2018) analyzed event-scale rainfall and flood processes in 163 catchments in Switzerland, and found that flash floods with steep rising and falling limbs of hydrographs were generally triggered by high total rainfall amount and maximum hourly rainfall. Fischer *et al*. (2019) compared flood-inducing rainfall characteristics between distinct flood types based on timescales (i.e., ratio between flood volume and flood peak) in Mulde River basin in eastern Germany, and noticed that flash floods are induced by rainfall processes with high intensity. Zheng *et al*. (2022) assessed effects of rainfall peak characteristics on flood hydrographs in Daqinghe catchment in China, and found that rainfall peak occurrence moment and rainfall peak number affected time to flood peak and shape of flood peak hydrographs, respectively. Present studies focus on certain rainfall temporal characteristics (e.g., rainfall amount and peak), while the attention on overall rainfall temporal distribution is insufficient. It is crucial to focus on the overall rainfall temporal structures (e.g., magnitude, intensity, time, and concentration), which can provide an effective approach to explore the generation and evolution mechanisms of flash floods.

Hydrological models, which usually adopt generalized mathematical equations to describe natural rainfall-flood processes, are powerful tools to probe the regularities of rainfall-runoff conversion and flood propagation (Wagener *et al*., 2001; Song *et al*., 2011; Zhang *et al*., 2021; Chen *et al*., 2023; Gao *et al*., 2023). Considering the accumulation of hydro-climatic and geomorphologic data as well as the concurrent maturation of computing power, hydrological models have been widely employed to develop effective flash flood hazard prediction plans (Liu and Liu, 2001; Meresa *et al*., 2021). The rigorous evaluation of model performance is useful for facilitating the applicability and effectiveness of hydrological models in operational forecasting and warning of flash floods. Rozalis *et al*. (2010) used an uncalibrated hydrological model, which was based on SCS curve number method and kinematic wave method, to simulate 20 flood events in Merhavia catchment in Israel, and found good model performances for flood events with high magnitudes and poor model performances for events with medium and low magnitudes. Orth *et al*. (2015) assessed simulation performances of HBV, PREVAH, and SWBM in eight well-observed catchments in Switzerland,

and found that all the three models fitted slightly better with observations at low altitude sites than those at high altitudes, and each model had its own unique advantages in flood simulation. McMillan *et al*. (2016) adopted TopNet to simulate daily rainfall-flood events in 485 catchments in New Zealand, and found better performances in larger and medium-wet catchments with smaller seasonal variations. To date, many studies have been conducted to assess model simulation capabilities with respect to catchments with different hydrological conditions or flood events with different characteristics. Whereas, the effects of rainfall temporal variability, which serves as the key factor inducing flash floods, on flash flood modelling are still ambiguous.

This study aims to identify the rainfall temporal patterns and associated flash flood behaviors in small mountainous catchments, and assess their effects on flash flood simulation performances. Two widely used hydrological models (i.e., XAJ and CNFF) in China are adopted for exploration. The specific objectives of this study include: (1) cluster typical rainfall types based on six rainfall temporal characteristic indices measuring magnitude, intensity, time, and concentration by principal component analysis and dynamic *K*-means cluster analysis; (2) identify flash flood process variations from perspective of six behavior indices induced by different rainfall temporal patterns; (3) assess model simulation capability under various rainfall types in reproducing water balances and flood hydrographs, as well as flash flood peak and dynamics behavior indices.

2 Study area and data sources

Anhe catchment (114°17′E–114°32′E, 25°56′N–26°70′N) located in southeastern China is selected for study with a drainage area of 251 km^2 (Figure 1). The study area belongs to a subtropical humid monsoon climate. The annual average rainfall is 1400 mm, 70% of which falls between April and September. The altitude decreases from northwest to southeast, with an average elevation of 492 m. The main land use types are forest (78.81%) and farmland (12.43%), and main soil texture types are sandy clay (80.24%) and sandy loam (10.12%).

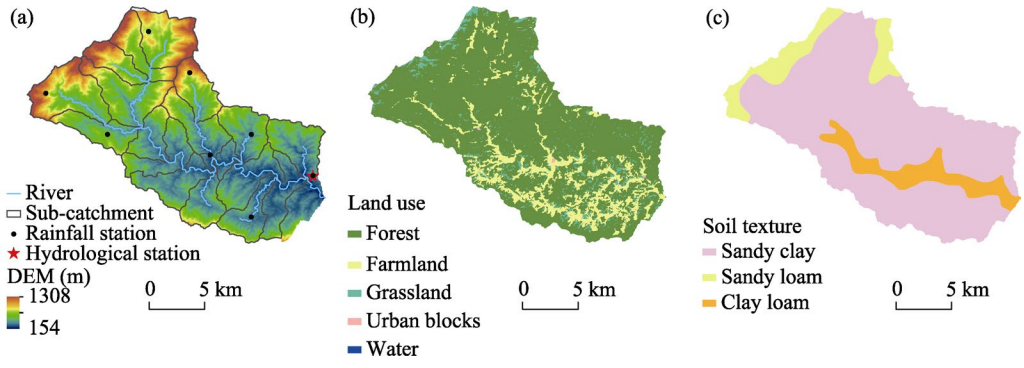

Figure 1 Spatial distribution of DEM and water system (a), land use (b) and soil texture types (c) in Anhe catchment

The collected dataset includes geographic information system (GIS) data as well as rainfall and water discharge observations. GIS data including digital elevation model (DEM, 1:50,000), river system (1:100,000), land use (1:250,000) and soil texture types (1:500,000),

is used for the delineation and attribute extraction of sub-catchments, all of which are collected from the National Geomatics Center of China (http://www.ngcc.cn/). The hourly rainfall and water discharge observations from 1978 to 2012 are collected from eight rainfall stations and Anhe hydrological station, and are used for rainfall type identification and model performance evaluation.

3 Methods

3.1 Rainfall type identification

3.1.1 Rainfall characteristic indices and flash flood behavior indices

A rainfall event is determined with its total rainfall amount threshold being 12.70 mm and the inter-event time threshold being 6 hours (Huff, 1967; Fan, 2012). Six rainfall characteristic indices are selected to describe the magnitude, intensity, time, and concentration of rainfall events (dos Santos *et al*., 2017; Park *et al*., 2019) (Table 1). Specifically, the peak rainfall moment coefficient (R_{MPI}) ranging from 0 to 1, describes the occurrence moment of peak rainfall, and a great value of R_{MPI} indicates a late occurrence moment of peak rainfall. The rainfall concentration (*PCI*) ranging from 0 to 1, describes the temporal distribution of hourly rainfall amounts, and a great value of *PCI* indicates high concentration of a rainfall temporal process.

Table 1 Selected rainfall characteristic indices at event scale

Category	Index	Abbreviation	Unit	Equation
Magnitude	Total rainfall amount	P	mm	$P=\sum_{t=F_{begin}}^{F_{end}} p_t$
	Average rainfall amount	AP	mm	$AP=P/T$
Intensity	Maximum rainfall intensity	MPI	mm/h	$MPI=\max(P_t)$
Time	Rainfall duration	T	h	$T=F_{end}-F_{begin}+1$
	Peak rainfall moment coefficient	R_{MPI}	–	$R_{MPI}=F_{MPI}/T$
Concentration	Rainfall concentration	PCI	–	$PCI=MPI/P$

Notes: p_t is the rainfall amount at time t, mm; F_{begin} and F_{end} are the time when a rainfall event begins and ends, respectively, h; F_{MPI} is the occurrence time of the maximum rainfall intensity, h.

Rainfall variability strongly impacts runoff generation and confluence processes of natural catchments. A flood event corresponding to the rainfall event is determined with its flood peak higher than the annual average water discharge and the inter-event time threshold being 6 hours. Six flash flood behavior indices, which are categorized into flood peak and dynamics indices, are used to characterize flood process variations induced by a certain rainfall pattern (Table 2) (Zhai *et al*., 2021a). Specifically, the average rates of rising and declining limbs (i.e. *RQ* and *DQ*) are used to quantify the change rates of flood discharges, and great values of *RQ* and *DQ* indicate quick onset and recession of a flood process, respectively. The flood hydrograph kurtosis (*K*) is used to quantify the shape of a flood hydrograph, and a great value of *K* indicates a thin flood hydrograph.

Table 2 Selected flash flood behavior indices at event scale

Category	Index	Abbreviation	Unit	Equation
Peak	Peak flow modulus	*Km*	$m^3/(s\cdot km^2)$	$Km=Q_m/A$
	Peak flow occurrence time	*Tm*	h	$Tm=T(Q_m)$
	Lag time	*Tl*	h	$Tl=Tm-F_{MPI}$
Dynamics	Average rate of rising limb	*RQ*	s^{-1}	$RQ=\frac{3600\left(Q_m-Q_{begin}\right)}{\left(Tm-T_{begin}\right)\sum_{t=T_{begin}}^{T_{end}}Q_t}$
	Average rate of declining limb	*DQ*	s^{-1}	$DQ=\frac{3600\left(Q_m-Q_{end}\right)}{\left(T_{end}-Tm\right)\sum_{t=T_{begin}}^{T_{end}}Q_t}$
	Flood hydrograph kurtosis	*K*	–	$K=\frac{1}{N}\sum_{t=T_{begin}}^{T_{end}}\left(\frac{Q_t-\mu}{\sigma}\right)^4$

Notes: Q_m is the peak flow, m^3/s; A is the catchment area, km^2; Q_{begin}, Q_{end} and Q_t are the flood flows at time T_{begin}, T_{end} and t, respectively, m^3/s; T_{begin} and T_{end} are the time when a flood process begins and ends, respectively, h; μ and σ are the average value and standard deviation value of a flood process, respectively.

3.1.2 Principal component analysis

Rainfall characteristics indices might be correlated with each other, which may result in information overlapping. Pearson correlation analysis is performed in advance to test their relationships, and the principal component analysis (PCA) is adopted to reduce the dimensionality of six rainfall characteristic indices. The p rainfall characteristic indices from n rainfall events constitute the initial matrix $X=\{x_{ij}\}_{n\times p}$, and is normalized into the matrix $X^*=\{x_{ij}^*\}_{n\times p}$ and correlation matrix $R=\{r_{kt}\}_{p\times p}$. The eigenvalues ($\lambda_1\geqslant\lambda_2\geqslant\ldots\geqslant\lambda_p$) of matrix R are determined by resolving Equation 1 and the corresponding eigenvector is $\mu_j=\left(\mu_{1j},\mu_{2j},...,\mu_{pj}\right)^{\mathrm{T}}\left(j=1,2,...,p\right)$.

$$\left|\begin{pmatrix} r_{11} & r_{12} & \ldots & r_{1p} \\ r_{21} & r_{22} & \ldots & r_{2p} \\ \ldots & \ldots & \ldots & \ldots \\ r_{p1} & r_{p2} & \ldots & r_{pp} \end{pmatrix}\right| - \left|\begin{pmatrix} \lambda_1 & 0 & \ldots & 0 \\ 0 & \lambda_2 & \ldots & 0 \\ \ldots & \ldots & \ldots & \ldots \\ 0 & 0 & \ldots & \lambda_p \end{pmatrix}\right| = 0 \quad (1)$$

where r_{kt} is the correlation coefficient between the kth and tth rainfall characteristic indices, k=1, 2,…, p, t=1, 2,…, p.

The objective function J is to preserve the variance information of original rainfall indices in maximum, and is expressed as Equation 2. The m PCA components are further determined if the cumulative variance $\left(\sum_{u=1}^{m}\lambda_u/\sum_{u=1}^{p}\lambda_u\right)$ is over 85%, and the PCA component matrix $P^*=\{z_{ij}\}_{n\times m}$ is obtained by Equation 3.

$$J\left(P^*\right)=\max\left[\sum_{u=1}^{m}Var\left(P_u\right)\right] \quad (2)$$

$$z_{ij} = \sum_{t=1}^{p} x_{it}^{*} \mu_{tj} \tag{3}$$

where P_u is the uth PCA component; $Var(P_u)$ is the variance of P_u; m is the number of selected PCA components; z_{ij} is the jth PCA component value of the ith rainfall event; x_{it}^{*} is the tth normalized rainfall characteristic index value of the ith rainfall event; μ_{ij} is the tth element of the jth eigenvector.

3.1.3 Dynamic *K*-means cluster analysis

The dynamic *K*-means cluster algorithm is implemented on the m PCA components to identify typical rainfall types. To minimize the total within-cluster variance sum (Var_{total}), the objective function J_c is denoted as Equation 4. Specifically, the similarities between rainfall events and cluster centroids are quantified using Euclidean distance d. Rainfall events are assigned into the cluster with the smallest d, and the averages of rainfall events within K clusters are considered as the new K cluster centroids to drive the next reassignment. The assignment calculation proceeds iteratively until the values of cluster centroids no longer change or change within a permitted narrow range, and all rainfall events are finally clustered into K typical rainfall types.

$$\begin{cases} J_c\left(\boldsymbol{U}^{*}, \boldsymbol{C}^{*}\right) = \min\left(\sum_{i=1}^{n}\sum_{r=1}^{K} \eta_{ir} d_{ir}^{2}\right) \\ d_{ir} = \sqrt{\sum_{j=1}^{m}\left(z_{ij} - c_{rj}\right)^{2}} \end{cases} \tag{4}$$

where U^{*} and C^{*} are the optimal partition matrix and the optimal cluster centroid matrix, respectively; K is the number of clusters; n is the number of rainfall-flood events; η_{ir} is the membership coefficient, $\eta_{ir} = \begin{cases} 0, & Z_i \notin r\text{th cluster} \\ 1, & Z_i \in r\text{th cluster} \end{cases}$; d_{ir} is the Euclidean distance between the ith rainfall event $Z_i = \left(z_{i1}, z_{i2}, ..., z_{im}\right)$ and the rth cluster centroid $C_r = \left(c_{r1}, c_{r2}, ..., c_{rm}\right)$; c_{rj} is the jth feature of C_r, $c_{rj} = \dfrac{\sum_{i=1}^{n} \eta_{ir} z_{ij}}{\sum_{i=1}^{n} \eta_{ir}}$.

The elbow method is adopted to assess the cluster performance (Thorndike, 1953). Both the value and the decreasing rate of Var_{total} decrease along with the increase of cluster number K, revealing that for a greater K the total within-cluster cohesion is improved and the cohesion improvement efficiency decreases simultaneously. The optimal cluster number K is determined based on the cohesion improvement efficiency. If the decreasing rate of Var_{total} decreases considerably beyond a certain cluster number, the number is considered to be a good choice, which occurs at the elbow inflection point of the curve between Var_{total} and K. Moreover, the Kruskal-Wallis test is adopted to examine whether the differences among the identified rainfall types are significant in terms of six rainfall characteristic indices (Theodorsson-Norheim, 1986).

3.2 Flash flood simulation

3.2.1 XAJ hydrological model

Xinanjiang hydrological model (XAJ) is developed by Professor Zhao Renjun of Hohai University (Zhao, 1992), and has been widely applied in humid and semi-humid regions for rainfall-runoff simulation and forecasting in China (Jie *et al*., 2018; Gong *et al*., 2021; Jiang *et al*., 2023). The tension and free water storage capacity curves are used to calculate runoff generation shown as Equation 5, and the linear reservoir method and the segmental Muskingum method are used to simulate overland runoff concentration and flood routing, respectively.

$$\begin{cases} \alpha = 1 - \left(1 - \dfrac{WM}{WMM}\right)^{B} \\ \beta = 1 - \left(1 - \dfrac{SM}{SMM}\right)^{EX} \end{cases} \tag{5}$$

where α is the proportion of the area with tension water storage capacity no greater than WM; β is the proportion of the area with free water storage capacity no greater than SM; WM and WMM are the tension water storage capacity within the study area and its maximum, respectively; SM and SMM are the free water storage capacity within the study area and its maximum, respectively; B and EX are the exponents.

3.2.2 CNFF hydrological model

China Flash Flood hydrological Model (CNFF) is developed by China Institute of Water Resources and Hydropower Research, and has been widely used in the simulation and early-warning of flash floods over China (Zhai *et al*., 2018; 2021b). In this study, the excess saturation runoff method is used to calculate runoff generation, the modified distributed unit hydrograph method and the dynamic Muskingum method are used to simulate overland runoff concentration and flood routing, respectively. The flow velocity and flow time of overland runoff are calculated as follows:

$$\begin{cases} V = KS^{0.5} i^{0.4} \\ T_j = \sum_{m=1}^{M_j} \dfrac{cL_m}{V_m} \end{cases} \tag{6}$$

where V is the flow velocity at a grid cell (25 m×25 m); K is the flow velocity coefficient, mainly affected by land use conditions (Soil Conservation Service, 1972); S is the hydraulic slope; i is the dimensionless rainfall intensity; T_j is the flow time from grid cell j to catchment outlet; L_m is the flow path length of water drops at the mth grid cell; c=1 or $\sqrt{2}$; M_j is the grid cell numbers along the flow path at grid cell j.

3.2.3 Model performance evaluation

The study area was divided into 19 sub-catchments, with an average drainage area of 13.16 km^2. The study period was evenly divided into three sub-periods: the first sub-period from 1978 to 1993 (36 rainfall-flood events in total) and last sub-period from 2001 to 2010 (36 rainfall-flood events in total) were set as model calibration period, and the second sub-period from 1994 to 2001 (35 rainfall-flood events in total) was set as model validation period. The objective function for parameter optimization was to minimize the average rela-

tive error of runoff volume (*RER*) and maximize the average Nash-Sutcliffe efficiency coefficient (*NSE*). The equations were expressed as follows. A small value of absolute *RER* indicates a well-obtained water balance between simulated and observed runoff volume, and a great value of *NSE* indicates a close agreement between simulated and observed flood hydrographs.

$$RER = \frac{1}{n}\sum_{j=1}^{n}\left(\frac{\overline{R}_{s,j} - \overline{R}_{o,j}}{\overline{R}_{o,j}}\right) \tag{7}$$

$$NSE = \frac{1}{n}\sum_{j=1}^{n}\left(1 - \frac{\sum_{t=1}^{N_j}\left(Q_{t,s,j} - Q_{t,o,j}\right)^2}{\sum_{t=1}^{N_j}\left(Q_{t,o,j} - \overline{Q}_{o,j}\right)^2}\right) \tag{8}$$

where $\overline{R}_{o,j}$ and $\overline{R}_{s,j}$ are the average observed and simulated runoff volume for the *j*th rainfall-flood event, respectively; $Q_{t,o,j}$ and $Q_{t,s,j}$ are the observed and simulated flood discharge at time *t* for the *j*th rainfall-flood event, respectively; $\overline{Q}_{o,j}$ is the average observed flood discharge for the *j*th rainfall-flood event; *n* is the number of rainfall-flood events; N_j is the length of *j*th rainfall-flood event.

Moreover, model performances on flash flood behavior indices are evaluated using the relative root mean square error (*RMSEr*) and linear correlation coefficient (*r*) with the optimal values of zero and one, respectively. A smaller *RMSEr* and a greater *r* indicate a better model performance on flash flood behavior indices. The evaluation indices are calculated as follows:

$$RMSEr = \sqrt{\frac{\sum_{i=1}^{n}(O_i - S_i)^2}{n \cdot \overline{O}^2}} \tag{9}$$

$$r = \frac{\sum_{i=1}^{n}\left(O_i - \overline{O}\right)\left(S_i - \overline{S}\right)}{\sqrt{\sum_{i=1}^{n}\left(O_i - \overline{O}\right)^2 \sum_{i=1}^{n}\left(S_i - \overline{S}\right)^2}} \tag{10}$$

where O_i and S_i are the observed and simulated flash flood behavior indices of the *i*th flood event; $\overline{O}$ and $\overline{S}$ are the average observed and simulated flash flood behavior indices for all events.

4 Results

4.1 Rainfall temporal pattern and associated flash flood behavior identification

There were 107 rainfall-flood events determined for rainfall type identification with total rainfall amount and inter-event time greater than 12.70 mm and 6 hours, respectively. Significant linear correlations existed between most of the rainfall characteristic indices (Figure 2). *P* was significantly and linearly correlated with *T* ($r \geqslant 0.50$, $p<0.05$), *AP* was significantly and linearly correlated with *MPI*, *T*, and *PCI* ($|r| \geqslant 0.50$, $p<0.05$), and *PCI* was also significantly and linearly correlated with *MPI* and *T* ($|r| \geqslant 0.50$, $p<0.05$).

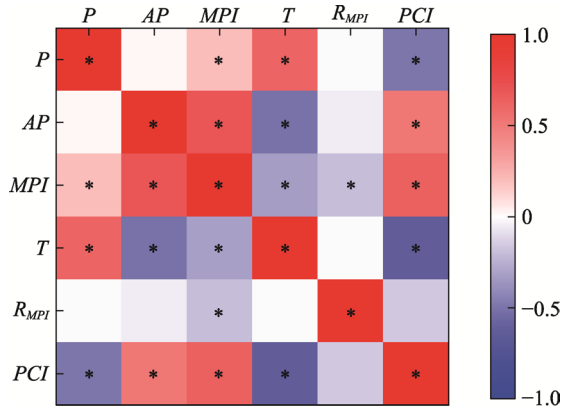

Figure 2 Correlation coefficients of rainfall characteristic indices
Note: * indicates the correlation coefficient has a significance level $p<0.05$.

Six rainfall characteristic indices were composited into three independent PCA components, which could explain 88.17% of the total rainfall characteristic variations. The first PCA component mainly included *AP*, *MPI*, *T* and *PCI*, the second PCA component mainly included *P*, and the third PCA component mainly included R_{MPI}. Specifically, these PCA components could explain 46.64%, 25.11% and 16.42% of the total variability, respectively. Dynamic *K*-means cluster analysis was then performed with cluster numbers ranging from one to eight. As shown in Figure 3, the total within-cluster variance sum (Var_{total}) decreased along with the increase of cluster number *K*, and the decreasing rate change of Var_{total} reached the maximum of –85.81 at *K*=3, after which the cohesion improvement efficiency began to decrease considerably. Thus, all rainfall events were clustered into three types, noted as Type 1, Type 2, and Type 3, with 14, 65, and 28 rainfall events, respectively. Furthermore, the Kruskal-Wallis test showed that the distributions of six rainfall characteristic indices existed significant differences among three rainfall types at a level of $p<0.01$, revealing that the identified rainfall types were significantly different.

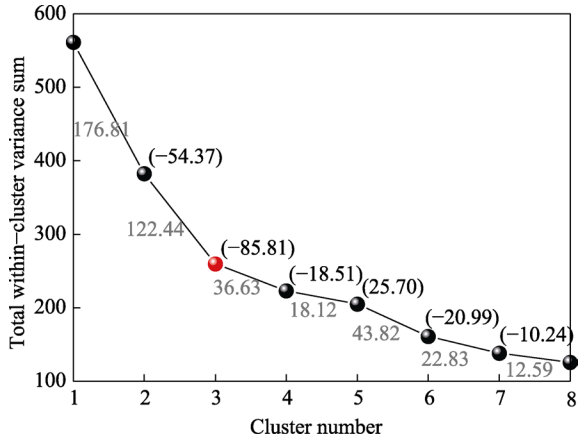

Figure 3 The diagram of total within-cluster variance sum (Var_{total}) versus cluster number (*K*)
Notes: The number on the broken line between *K*=*i* and *K*=*i*+1 ($1 \leqslant i \leqslant 7$) represents the decreasing rate of Var_{total} with *K* increasing from *i* to *i*+1, which is noted as $Var_{total}(i)^{*}$. The number within the bracket represents the difference between $Var_{total}(i+1)^{*}$ and $Var_{total}(i)^{*}$, which is noted as $Var_{total}(i+1)^{\#}$. The red point represents the optimal cluster number *K*, which is the elbow inflection point of the curve with the minimum $Var_{total}(K=3)^{\#}$.

The characteristics of three rainfall types were distinct from each other (Figure 4). The average values of *P*, *AP*, *MPI*, *T*, R_{MPI} and *PCI* were 56.94 mm, 8.09 mm, 30.14 mm/h, 7.93 h, 0.39, and 0.55, respectively for Type 1; 50.19 mm, 2.84 mm, 12.24 mm/h, 21.06 h, 0.46, and 0.27, respectively for Type 2; 115.68 mm, 2.32 mm, 12.43 mm/h, 54.04 h, 0.49, and 0.10, respectively for Type 3. Type 1 was characterized by small total amount, high intensity, short duration, early peak moment, and concentrated hourly distribution. Type 3 was characterized by great total amount, low intensity, long duration, late peak moment, and relatively uniform hourly distribution. The characteristics of Type 2 laid between those of Type 1 and Type 3.

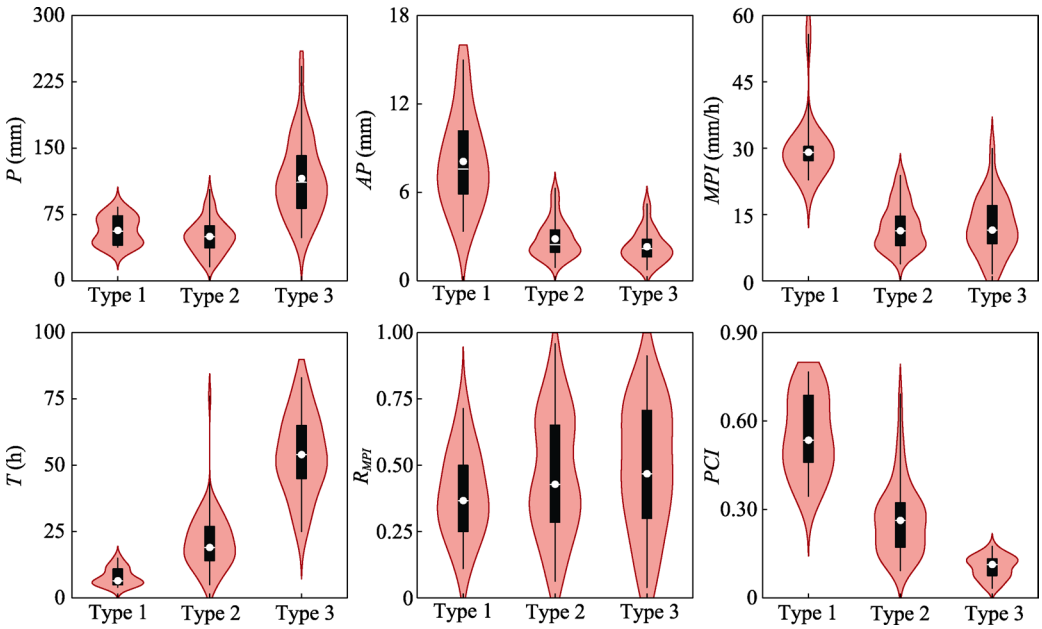

Figure 4 Distribution of rainfall characteristic indices for three rainfall types

Notes: Boxes represent the ranges from the 25th to the 75th quartiles, whiskers represent the ranges from the minimum to the maximum, and dots and lines in boxes represent the averages and the medians, respectively.

As for the flash floods induced by the three rainfall types, flash flood behavior indices were closely related with rainfall characteristic indices (Figure S1) and varied greatly among type to type (Figure 5). Specifically, *Km* showed significant correlations with R_{MPI} and *PCI* for Type 1, with *P* for Type 2, and with *P*, *AP* and *MPI* for Type 3 ($|r| \geqslant 0.50$, $p<0.05$). *Tm* showed significant correlation with R_{MPI} for Type 1 ($r \geqslant 0.50$, $p<0.05$). *Tl* showed significant correlation with *MPI* for Type 1 ($r \leqslant -0.50$, $p<0.05$). *RQ* showed significant correlations with *MPI* for Type 1, with *AP* for Type 2, and with *AP*, *MPI* and *PCI* for Type 3 ($r \geqslant 0.50$, $p<0.05$). *DQ* showed significant correlations with *AP* and *MPI* for Type 3 ($r \geqslant 0.50$, $p<0.05$). *K* showed significant correlations with *P* and *PCI* for Type 1 ($|r| \geqslant 0.50$, $p<0.05$). The average values of *Km*, *Tm*, *Tl*, *RQ*, *DQ* and *K* were 0.48 $m^3/(s \cdot km^2)$, 4.99 h, 3.71 h, 41.54 s^{-1}, 13.52 s^{-1}, and 3.37, respectively for Type 1; 0.37 $m^3/(s \cdot km^2)$, 9.13 h, 5.10 h, 21.76 s^{-1}, 8.64 s^{-1}, and 3.56, respectively for Type 2; 0.71 $m^3/(s \cdot km^2)$, 15.26 h, 5.44 h, 5.15 s^{-1}, 2.82 s^{-1}, and 3.23, respectively for Type 3. The flash floods induced by Type 1 were characterized by

small peak flow magnitude, early peak flow occurrence time, short lag time, rapid flood rising and declining rates, and thin flood hydrographs. The flash flood processes induced by Type 3 were characterized by great peak flow magnitude, late peak flow occurrence time, long lag time, slow flood rising and declining rates, and fat flood hydrographs. Similarly, the characteristics of Type 2 laid between those of Type 1 and Type 3.

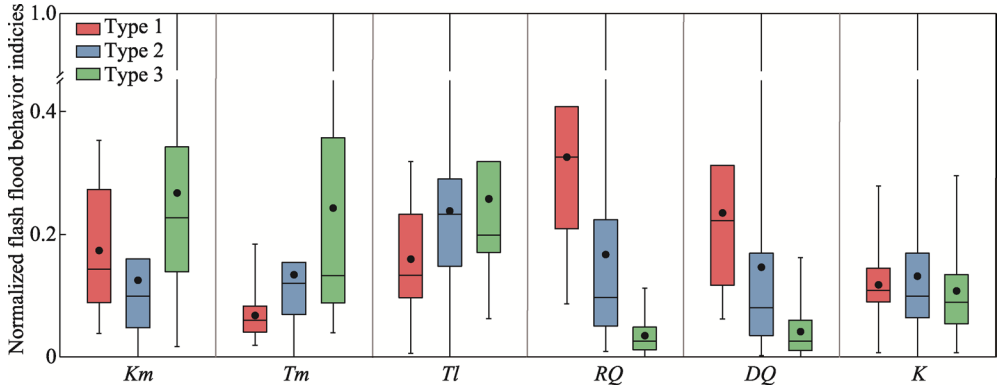

Figure 5 Distribution of normalized flash flood behavior indices induced by three rainfall types

Notes: The flash flood behavior indices are normalized using $Y^* = \frac{Y - Y_{min}}{Y_{max} - Y_{min}}$, where Y^* and Y are values before and after normalization, respectively; Y_{max} and Y_{min} are the maximum and the minimum, respectively. Boxes represent the ranges from the 25th to the 75th quartiles, whiskers represent the ranges from the minimum to the maximum, and dots and lines in boxes represent the averages and the medians, respectively.

4.2 Flash flood process simulation evaluation

The evaluation indices for flash flood simulations at event scale were shown in Table 3. As for XAJ, *RER* varied between –20.64% and 50.27% with an average absolute value of 6.89% in calibration period, and varied between –42.37% and 19.56% with an average absolute value of 10.62% in validation period. *NSE* varied between –0.22 and 0.97 with an average value of 0.78 in calibration period, and varied between 0.03 and 0.97 with an average value of 0.72 in validation period. As for CNFF, *RER* varied between –29.80% and 24.10% with an average absolute value of 7.58% in calibration period, and varied between –33.90% and 49.20% with an average absolute value of 18.58% in validation period. *NSE* varied between 0.44 and 0.98 with an average value of 0.87 in calibration period, and varied between 0.20 and 0.96 with an average value of 0.70 in validation period. Overall, model performances were consistent for XAJ and CNFF, both of which could well simulate water balances and flood hydrographs in the study area.

Table 3 Evaluation indices for flash flood process simulation

Model	Evaluation indices	Period		Type		
		Calibration	Validation	Type 1	Type 2	Type 3
XAJ	Absolute *RER* (%)	6.89	10.62	10.73	7.67	7.81
	NSE	0.78	0.72	0.79	0.71	0.85
CNFF	Absolute *RER* (%)	7.58	18.58	13.17	11.00	10.60
	NSE	0.87	0.70	0.76	0.81	0.85

The cumulative frequency distribution of absolute *RER* and *NSE* for three rainfall types is displayed in Figure 6, and the simulated and observed flash flood processes are displayed in Figure 7. XAJ and CNFF provided similar simulation performances for three rainfall types on water balances as well as flood hydrographs. For water balances, absolute *RER*s for most Type 1 events were greater than those for Type 2 and Type 3 events, and the average absolute *RER*s for both Type 2 and Type 3 were within 8.00% for XAJ and within 11.00% for CNFF (Table 3). Thus, the two models can better simulate water balances for Type 2 and Type 3 events than those for Type 1 events. For flood hydrographs, *NSE*s for Type 3 events were overall greater than those for Type 1 and Type 2 events, and hence both models could well capture flood hydrograph variations for Type 3 events with the average *NSE* reaching 0.85. Comparably, the agreement between observed and simulated hydrographs was the worst obtained by XAJ for Type 2 events (*NSE*=0.71) and by CNFF for Type 1 events (*NSE*=0.76), respectively. In addition, it was noted that CNFF generally over-estimated the flood recession rates of Type 1 events (e.g. events 19940503 and 20080524 in Figure 7), suggesting that CNFF was insufficient in reproducing the declining limb shape for quick-developing flood hydrographs.

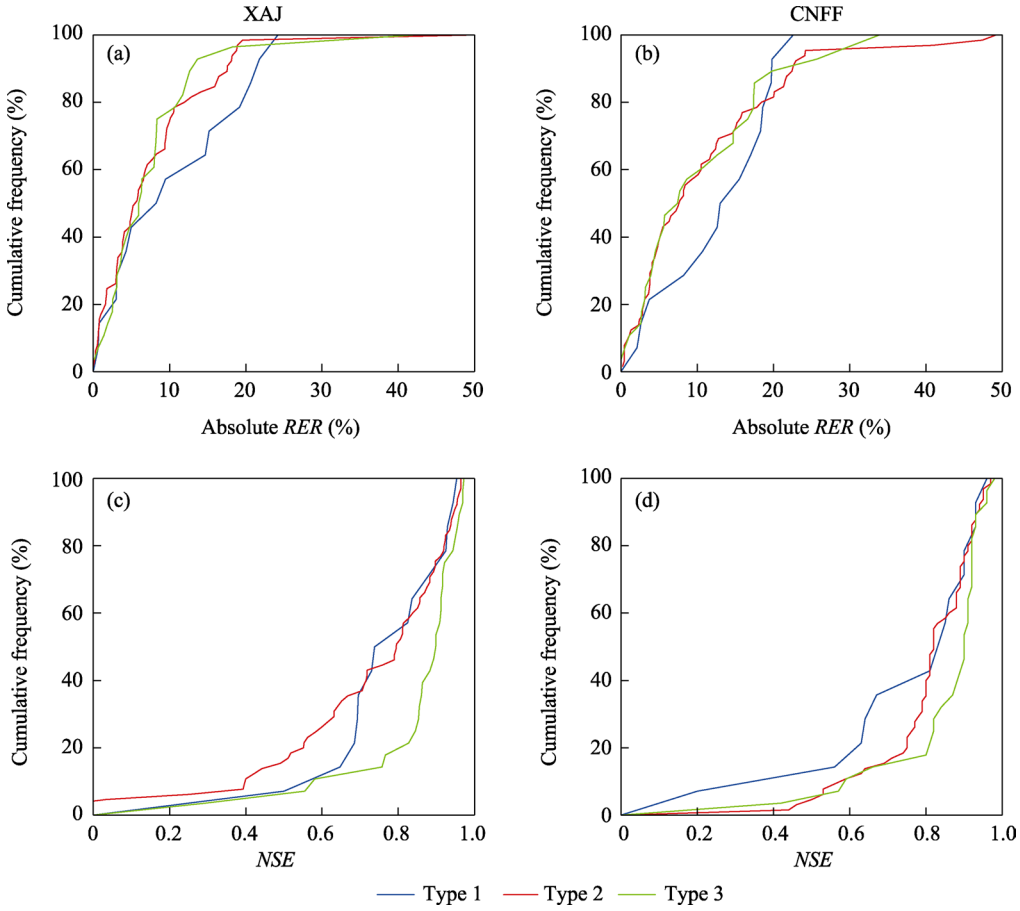

Figure 6 Cumulative frequency distribution of absolute *RER* and *NSE* for three rainfall types
Notes: (a) and (c) are the absolute *RER* and *NSE* by XAJ, (b) and (d) are the absolute *RER* and *NSE* by CNFF.

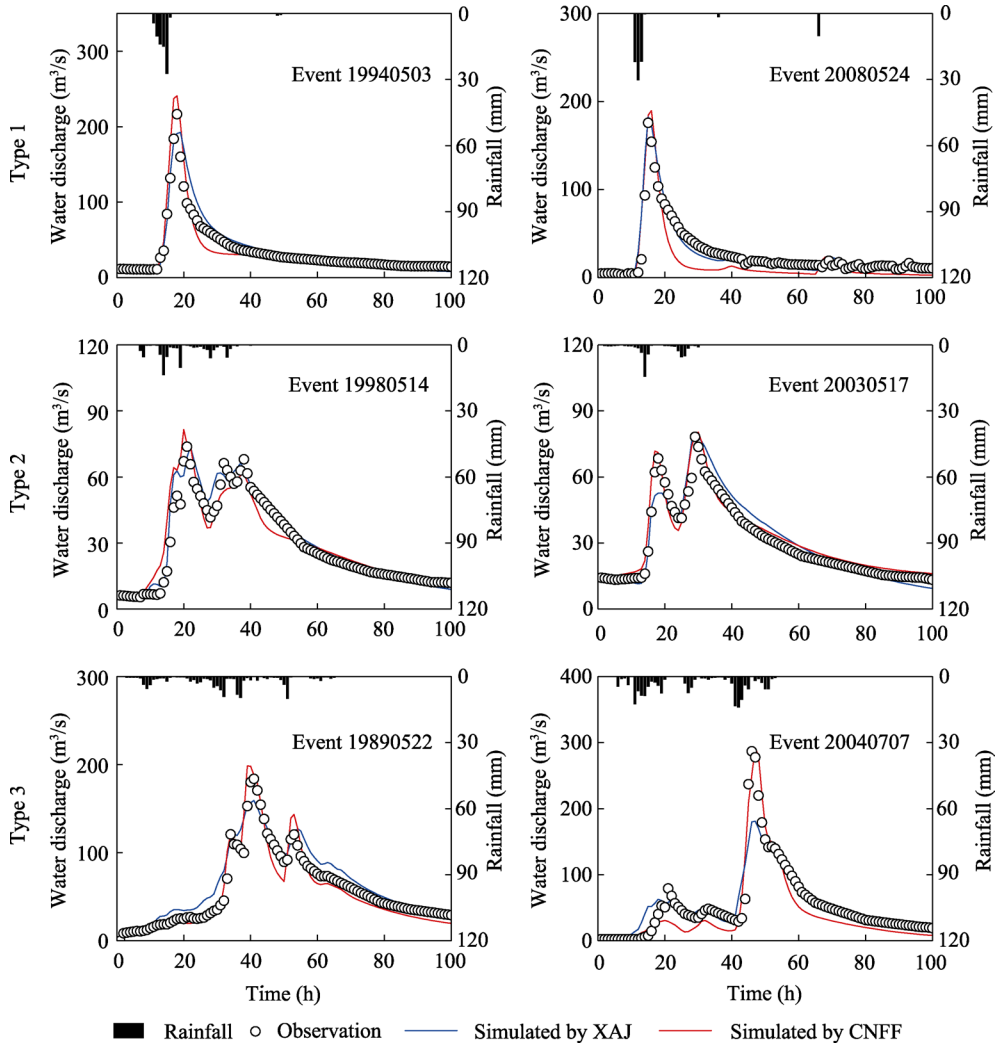

Figure 7 Observed and simulated flash flood processes of partial events

4.3 Flash flood behavior simulation evaluation

Both XAJ and CNFF reasonably reproduced the flash flood behaviors of 107 events in study area, with most of the observed and simulated behavior indices fitting the 1:1 line well (Figure 8). Table 4 listed the evaluation indices for flash flood behavior simulation.

For all flash flood behavior indices, the average *RMSEr* and *r* ranged from 0.29 (Type 3) to 0.38 (Type 2) and from 0.67 (Type 1) to 0.90 (Type 3), respectively for XAJ, and ranged from 0.24 (Type 3) to 0.31 (Type 1 and Type 2) and from 0.68 (Type 1) to 0.95 (Type 3), respectively for CNFF. The model performances of XAJ and CNFF shared a similarity in simulating flood behaviors for three rainfall types. All flash flood behavior indices for Type 3 were the best simulated with the smallest deviation and strongest linear correlation, while those for Type 1 were simulated with the weakest linear correlation and those for Type 2 were simulated with the greatest deviation.

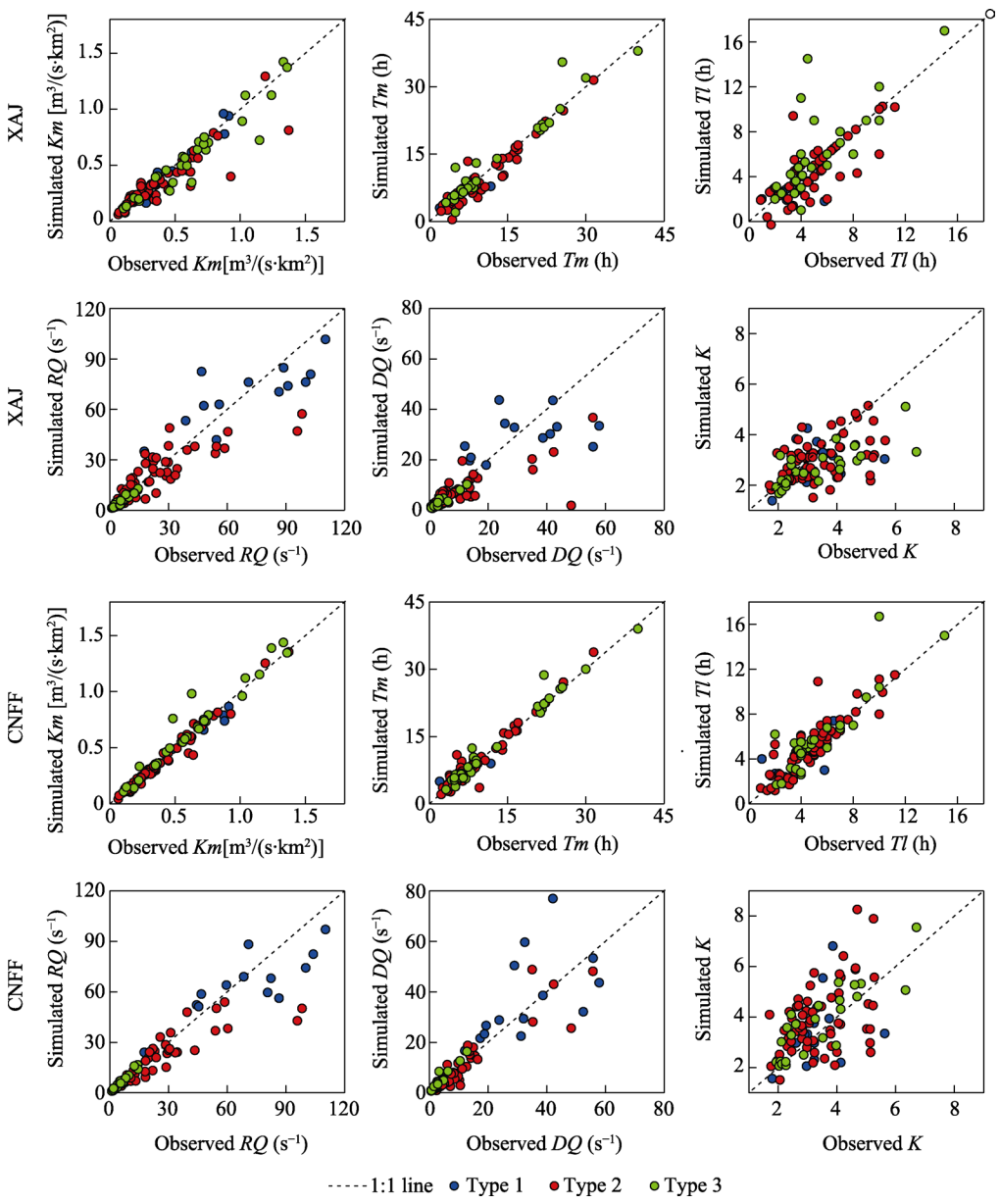

Figure 8 Observed and simulated flash flood behavior indices for XAJ and CNFF

For flood peak indices, the average *RMSEr* and *r* ranged from 0.26 (Type 1) to 0.28 (Type 2 and Type 3) and from 0.85 (Type 1) to 0.90 (Type 2 and Type 3), respectively for XAJ, and ranged from 0.20 (Type 2 and Type 3) to 0.23 (Type 1) and from 0.85 (Type 1) to 0.95 (Type 2 and Type 3), respectively for CNFF. As for XAJ, flood peak indices for Type 1 were simulated with smaller deviation but weaker linear correlation than those for Type 2 and Type 3. As for CNFF, flood peak indices for Type 2 and Type 3 were simulated with smaller deviation and stronger linear correlation than those for Type 1. Therefore, XAJ competitively simulated flood peak indices induced by three rainfall types, and CNFF better simulated those induced by Type 2 and Type 3.

Table 4 Evaluation indices for flash flood behavior simulations

Model	Evaluation indices	Type	Flash flood behavior indices					
			Km	*Tm*	*Tl*	*RQ*	*DQ*	*K*
XAJ	*RMSEr*	Type 1	0.15	0.26	0.35	0.27	0.44	0.35
		Type 2	0.33	0.18	0.33	0.43	0.55	0.43
		Type 3	0.18	0.18	0.49	0.23	0.33	0.33
	r	Type 1	0.96	0.89	0.70	0.79	0.46	0.23
		Type 2	0.90	0.96	0.85	0.85	0.85	0.39
		Type 3	0.97	0.98	0.73	0.96	0.97	0.75
CNFF	*RMSEr*	Type 1	0.11	0.25	0.34	0.30	0.44	0.40
		Type 2	0.12	0.16	0.29	0.36	0.55	0.36
		Type 3	0.18	0.11	0.31	0.20	0.40	0.24
	r	Type 1	0.99	0.86	0.69	0.67	0.56	0.32
		Type 2	0.99	0.97	0.90	0.93	0.89	0.61
		Type 3	0.98	0.99	0.88	0.98	0.99	0.86

Compared with flood peak indices, the simulation performances of both XAJ and CNFF declined for flood dynamics indices (Figure 8). The average *RMSEr* and *r* of flood dynamics indices ranged from 0.30 (Type 3) to 0.47(Type 2) and from 0.49 (Type 1) to 0.90 (Type 3), respectively for XAJ, and ranged from 0.28 (Type 3) to 0.42 (Type 2) and from 0.52 (Type 1) to 0.94 (Type 3), respectively for CNFF. XAJ and CNFF also shared a similar performance pattern for three rainfall types in terms of flood dynamics behavior simulation like the simulation for all flood behaviors. Flood dynamics indices for Type 3 were the best simulated with the smallest deviation and the strongest linear correlation, while those for Type 1 were simulated with the weakest linear correlation and those for Type 2 were simulated with the greatest deviation.

5 Discussion

Rainfall temporal characteristics play a dominant role in runoff generation and concentration processes. It is of considerable interest for regional flash flood management to identify flash flood behavior characteristics and evaluate model simulation capability with respect to different rainfall temporal patterns. This study proposes a rainfall temporal pattern identification method taking the magnitude, intensity, time, and concentration features of rainfall processes all into account, which not only is operable and feasible for practical implementation and is generalizable for catchments with massive rainfall-flood events, but also thoroughly considers rainfall characteristics probably affecting flood behaviors.

The defined 107 rainfall events in Anhe catchment were identified into three typical rainfall types (Type 1, Type 2, and Type 3), and the temporal variability of rainfall types and inducing flash flood behaviors shared great consistency. Type 1 rainfall events, which mainly occur in May (nearly 40% of rainfall events), are mainly generated in convective rainfall weather systems (Zhang *et al*., 2011). Although the total rainfall amount is small, Type 1 rainfall events with short duration, heavy intensity, and concentrated hourly distribution tend to induce flash floods with rapid flood rising and declining rates as well as thin flood hydro-

graphs. These conspicuous flash flood behavior characteristics imply that Type 1 rainfall-flood events are of strong instantaneous destructive power and pose great challenges for flash flood warning and forecasting, which may result in poor timeliness of flood warning information, insufficient time to coordinate flood response measures, and damages to human lives and properties (Ruiz-Villanueva *et al*., 2012; Archer and Fowler, 2018). Type 3 rainfall events, which occur throughout the year, are mainly generated in frontal rainfall weather systems (Zhang and Hall, 2004). Although the rainfall intensity is low, this rainfall type with great total amount, long duration and relatively uniform hourly distribution generally induces flash floods with great peak magnitude and runoff volume, which is likely to cause inundation risks to riparian villages. The inducing weather systems of Type 2 are the couple of those of Type 1 and Type 3, rather than a single dominant weather system type. The temporal characteristics of both rainfall events and corresponding flash floods for Type 2 lie between those of Type 1 and Type 3, as well as the hazard and destructiveness of flood events. Therefore, flood management strategies should be formulated considering rainfall processes with different temporal structures to implement timely and effective flash flood disaster prevention actions.

XAJ and CNFF both well reproduce the hourly variability of flood process in the study area and provide similar simulation performances for three rainfall types. Comparably, Type 3 events are the best simulated for both flood processes and flood behaviors, while Type 1 and Type 2 events are simulated less satisfactorily. The simulation differences reveal that both XAJ and CNFF show superiority in capturing variations of flood process induced by rainfall with long duration and relatively uniform hourly distribution, while they are still insufficient for floods induced by rainfall with short duration and concentrated hourly distribution. In mountainous catchments, rainfall with high intensity that exceeds infiltration capacity of soil can cause overland flow even though soil moistures are not saturated (Uhlenbrook and Leibundgut, 2002; Berghuijs *et al*., 2016), which is referred to as the excess infiltration runoff generation. As for Type 1 characterized by relatively high intensity and concentration, the existence of excess infiltration runoff mechanism, which is inconsistent with the underlying theories of XAJ and CNFF, might result in the discrepancy between calculated and actual runoff yielding (Zhai *et al*., 2021b), and subsequently affect model capability for reproducing flood hydrograph variability (e.g., flood hydrograph kurtosis). Besides, Type 1 and Type 2 events are both of short durations and great variations in temporal distributions, and the hourly rainfall observations are deficient in describing the temporal rainfall variability in detail (Bonaccorso *et al*., 2020). It may be inferred that lack of precise rainfall forcing may also be the key factor restricting the simulation performances of two models for quick flood responses induced by Type 1 and Type 2. In order to further improve model simulation capability especially for Type 1 and Type 2, accurate rainfall forcing in both space and time should be collected to well depict the magnitude, intensity, time, and temporal distribution of rainfall processes, and runoff generation modules of both XAJ and CNFF should be improved to well capture variations of thin flood hydrographs generated under rainfall events with high intensity and concentration. Model parameters might be optimized for various rainfall temporal patterns to further improve flash flood simulation accuracy. Furthermore, it is remarkable that CNFF outperforms XAJ in simulating flood hydrographs for Type 2 and Type 3, as well as most flood behaviors for three rainfall types.

This phenomenon can be ascribed to the use of modified distributed unit hydrograph method for runoff concentration calculation in CNFF, which has advantages in portraying the non-linear characteristics of runoff confluence processes in mountainous catchments. However, CNFF needs to be improved to better obtain water balances induced by rainfall with different temporal variability, and reproduce overall flood hydrographs induced by short-duration heavy rainfall. Moreover, more events should be collected from various mountainous catchments with diverse rainfall characteristics in further studies to validate the flash flood simulation capability with respect to rainfall temporal variability.

6 Conclusions

In this study, the multivariate statistical analysis and hydrological simulations were combined to identify typical rainfall types and simulate flash flood processes from perspective of rainfall characteristic indices and flash flood behavior indices. The results showed that:

(1) Three typical rainfall types were identified from 107 rainfall events. Type 1 was characterized by small total amount, high intensity, short duration, early peak moment, and concentrated hourly distribution. Type 3 was characterized by great total amount, low intensity, long duration, late peak moment, and relatively uniform hourly distribution. The characteristics of Type 2 laid between those of Type 1 and Type 3.

(2) Both XAJ and CNFF showed satisfactory performances in simulating flash flood processes with average absolute *RER* within 19% and average *NSE* over 0.70 in both calibration and validation periods. Water balances and flood hydrographs were better reproduced by both models for Type 3 with average absolute *RER* within 11.00% and average *NSE* reaching 0.85.

(3) Both XAJ and CNFF reasonably reproduced most flash flood behavior indices for three rainfall types with average *RMSEr* within 0.40 and average *r* over 0.67. All the indices and flood dynamics indices were the best simulated by both models for Type 3 with average *RMSEr* within 0.30 and average *r* over 0.90. The flood peak indices were competitively simulated for all the three rainfall types by XAJ and except Type 1 by CNFF.

References

Archer D R, Fowler H J, 2018. Characterising flash flood response to intense rainfall and impacts using historical information and gauged data in Britain. *Journal of Flood Risk Management*, 11(Suppl.1): S121–S133.

Ashley S T, Ashley W S, 2008. Flood fatalities in the United States. *Journal of Applied Meteorology and Climatology*, 47(3): 805–818.

Barredo J I, 2007. Major flood disasters in Europe: 1950–2005. *Natural Hazards*, 42(1): 125–148.

Batisani N, 2011. Spatio-temporal ephemeral streamflow as influenced by climate variability in Botswana. *Journal of Geographical Sciences*, 21(3): 417–428.

Berghuijs W R, Woods R A, Hutton C J *et al*., 2016. Dominant flood generating mechanisms across the United States. *Geophysical Research Letters*, 43(9): 4382–4390.

Bonaccorso B, Brigandì G, Aronica G T, 2020. Regional sub-hourly extreme rainfall estimates in Sicily under a scale invariance framework. *Water Resources Management*, 34(14): 4363–4380.

Borga M, Anagnostou E N, Blöschl G *et al*., 2011. Flash flood forecasting, warning and risk management: The HYDRATE project. *Environmental Science & Policy*, 14(7): 834–844.

Brunner M I, Viviroli D, Furrer R *et al*., 2018. Identification of flood reactivity regions via the functional cluster-

ing of hydrographs. *Water Resources Research*, 54(3): 1852–1867.

Chen J X, Zhang J H, Peng J B *et al*., 2023. Alp-valley and elevation effects on the reference evapotranspiration and the dominant climate controls in Red River Basin, China: Insights from geographical differentiation. *Journal of Hydrology*, 620: 129397.

dos Santos J C N, de Andrade E M, Medeiros P H A *et al*., 2017. Effect of rainfall characteristics on runoff and water erosion for different land uses in a tropical semiarid region. *Water Resources Management*, 31(1): 173–185.

Fan Z H, 2012. Research on precipitation trend analysis and design storm of Tianjin city [D]. Beijing: Tianjin University. (in Chinese)

Fischer S, Schumann A, Bühler P, 2019. Timescale-based flood typing to estimate temporal changes in flood frequencies. *Hydrological Sciences Journal*, 64(15): 1867–1892.

Gao W, Liu Y, Du Z P *et al*., 2023. Hedging effect alleviates the impact of land use on mainstream hydrological regimes: Evidence from Jinsha River, China. *Journal of Geographical Sciences*, 33(10): 2011–2030.

Garambois P A, Larnier K, Roux H *et al*., 2014. Analysis of flash flood-triggering rainfall for a process-oriented hydrological model. *Atmospheric Research*, 137: 14–24.

Gong J F, Yao C, Li Z J *et al*., 2021. Improving the flood forecasting capability of the Xinanjiang model for small-and medium-sized ungauged catchments in South China. *Natural Hazards*, 106(3): 2077–2109.

Habibi A, Delavar M R, Sadeghian M S *et al*., 2023. A hybrid of ensemble machine learning models with RFE and Boruta wrapper-based algorithms for flash flood susceptibility assessment. *International Journal of Applied Earth Observation and Geoinformation*, 122: 103401.

Huff F A, 1967. Time distribution of rainfall in heavy storms. *Water Resources Research*, 3(4): 1007–1019.

Jiang X L, Zhang L P, Liang Z M *et al*., 2023. Study of early flood warning based on postprocessed predicted precipitation and Xinanjiang model. *Weather and Climate Extremes*, 42: 100611.

Jie M X, Chen H, Xu C Y *et al*., 2018. Transferability of conceptual hydrological models across temporal resolutions: approach and application. *Water Resources Management*, 32: 1367–1381.

Khajehei S, Ahmadalipour A, Shao W Y *et al*., 2020. A place-based assessment of flash flood hazard and vulnerability in the contiguous United States. *Scientific Reports*, 10(1): 448.

Leal M, Reis E, Santos P P, 2022. Exploring spatial relationships between stream channel features, water depths and flow velocities during flash floods using HEC-GeoRAS and geographic information systems. *Journal of Geographical Sciences*, 32(4): 757–782.

Liu Y H, Li Z J, Liu Z Y *et al*., 2022. Impact of rainfall spatiotemporal variability and model structures on flood simulation in semi-arid regions. *Stochastic Environmental Research and Risk Assessment*, 36(3): 785–809.

Liu R Y, Liu N, 2001. A GIS-based method for flooded area calculation and damage evaluation. *Journal of Geographical Sciences*, 11(2): 187–192.

Lompi M, Caporali E, Mediero L *et al*., 2022. Improving flash flood risk assessment using a simple approach for extreme rainfall scaling and storms transposition. *Journal of Flood Risk Management*, 15(3): e12796.

Meresa H, Murphy C, Fealy R *et al*., 2021. Uncertainties and their interaction in flood hazard assessment with climate change. *Hydrology and Earth System Sciences*, 25(9): 5237–5257.

McMillan H K, Booker D J, Cattoën C, 2016. Validation of a national hydrological model. *Journal of Hydrology*, 541: 800–815.

Orth R, Staudinger M, Seneviratne S I *et al*., 2015. Does model performance improve with complexity? A case study with three hydrological models. *Journal of Hydrology*, 523: 147–159.

Park J, Onof C, Kim D, 2019. A hybrid stochastic rainfall model that reproduces some important rainfall characteristics at hourly to yearly timescales. *Hydrology and Earth System Sciences*, 23(2): 989–1014.

Ritter J, Berenguer M, Corral C *et al*., 2020. ReAFFIRM: Real-time assessment of flash flood impacts: A regional high-resolution method. *Environment International*, 136: 105375.

Rozalis S, Morin E, Yair Y *et al*., 2010. Flash flood prediction using an uncalibrated hydrological model and radar rainfall data in a Mediterranean watershed under changing hydrological conditions. *Journal of Hydrology*, 394(1/2): 245–255.

Ruiz-Villanueva V, Borga M, Zoccatelli D *et al*., 2012. Extreme flood response to short-duration convective rainfall in South-West Germany. *Hydrology and Earth System Sciences*, 16(5): 1543–1559.

Soil Conservation Service, 1972. National Engineering Handbook (Section 4): Hydrology. Washington, DC: US Department of Agriculture.

Song X M, Zhan C S, Kong F Z *et al*., 2011. Advances in the study of uncertainty quantification of large-scale hydrological modeling system. *Journal of Geographical Sciences*, 21(5): 801–819.

Theodorsson-Norheim E, 1986. Kruskal-Wallis test: BASIC computer program to perform nonparametric one-way analysis of variance and multiple comparisons on ranks of several independent samples. *Computer Methods and Programs in Biomedicine*, 23(1): 57–62.

Thorndike R L, 1953. Who belongs in the family? *Psychometrika*, 18: 267–276.

Uhlenbrook S, Leibundgut C, 2002. Process-oriented catchment modelling and multiple-response validation. *Hydrological Processes*, 16(2): 423–440.

Wagener T, Boyle D P, Lees M J *et al*., 2001. A framework for development and application of hydrological models. *Hydrology and Earth System Sciences*, 5(1): 13–26.

Yin J, Gao Y, Chen R S *et al*., 2023. Flash floods: why are more of them devastating the world's driest regions? *Nature*, 615(7951): 212–215.

Zhai X Y, Guo L, Liu R H *et al*., 2018. Rainfall threshold determination for flash flood warning in mountainous catchments with consideration of antecedent soil moisture and rainfall pattern. *Natural Hazards*, 94(2): 605–625.

Zhai X Y, Guo L, Zhang Y Y, 2021a. Flash flood type identification and simulation based on flash flood behavior indices in China. *Science China*: *Earth Sciences*, 64(7): 1140–1154.

Zhai X Y, Zhang Y Y, Zhang Y Q *et al*., 2021b. Simulating flash flood hydrographs and behavior metrics across China: Implications for flash flood management. *Science of the Total Environment*, 763: 142977.

Zhang J Y, Hall M J, 2004. Regional flood frequency analysis for the Gan-Ming River basin in China. *Journal of Hydrology*, 296(1–4): 98–117.

Zhang R H, Ni Y Q, Liu L P *et al*., 2011. South China heavy rainfall experiments (SCHeREX). *Journal of the Meteorological Society of Japan*, 89A: 153–166.

Zhang Y, Wang Y, Chen Y *et al*., 2019. Assessment of future flash flood inundations in coastal regions under climate change scenarios: A case study of Hadahe River basin in northeastern China. *Science of the Total Environment*, 693: 133550.

Zhang Y Y, Chen Q T, Xia J, 2020. Investigation on flood event variations at space and time scales in the Huaihe River Basin of China using flood behavior classification. *Journal of Geographical Sciences*, 30(12): 2053–2075.

Zhang Y Y, Xia J, Shao Q X *et al*., 2021. Uncertainty analysis for integrated water system simulations using GLUE with different acceptability thresholds. *Science China Technological Sciences*, 64(8): 1791–1804.

Zhao R J, 1992. The Xinanjiang model applied in China. *Journal of Hydrology*, 135(1–4): 371–381.

Zheng Y C, Li J Z, Rong Y T *et al*., 2022. Quantification of rainfall spatial and temporal distribution characteristics on the flood hydrograph and its application in flood type classification. *Journal of Hydraulic Engineering*, 53(5): 560–573. (in Chinese)